JOURNAL OF GEOPHYSICAL RESEARCH, VOL. 99, NO. C4, PAGES 7433–7442, APRIL 15, 1994

# Time scales of pattern evolution from cross-spectrum analysis of advanced very high resolution radiometer and coastal zone color scanner imagery

Kenneth L. Denman
Department of Fisheries and Oceans, Institute of Ocean Sciences, Sidney, British Columbia, Canada

Mark R. Abbott
College of Oceanic and Atmospheric Sciences, Oregon State University, Corvallis

**Abstract.** We have selected square subareas (110 km on a side) from coastal zone color scanner (CZCS) and advanced very high resolution radiometer (AVHRR) images for 1981 in the California Current region off northern California for which we could identify sequences of cloud-free data over periods of days to weeks. We applied a two-dimensional fast Fourier transform to images after median filtering, $(x, y)$ plane removal, and cosine tapering. We formed autospectra and coherence spectra as functions of a scalar wavenumber. Coherence estimates between pairs of images were plotted against time separation between images for several wide wavenumber bands to provide a temporal lagged coherence function. The temporal rate of loss of correlation (decorrelation time scale) in surface patterns provides a measure of the rate of pattern change or evolution as a function of spatial dimension. We found that patterns evolved (or lost correlation) approximately twice as rapidly in upwelling jets as in the "quieter" regions between jets. The rapid evolution of pigment patterns (lifetime of about 1 week or less for scales of 50–100 km) ought to hinder biomass transfer to zooplankton predators compared with phytoplankton patches that persist for longer times. We found no significant differences between the statistics of CZCS and AVHRR images (spectral shape or rate of decorrelation). In addition, in two of the three areas studied, the peak correlation between AVHRR and CZCS images from the same area occurred at zero lag, indicating that the patterns evolved simultaneously. In the third area, maximum coherence between thermal and pigment patterns occurred when pigment images lagged thermal images by 1–2 days, mirroring the expected lag of high pigment behind low temperatures (and high nutrients) in recently upwelled water. We conclude that in dynamic areas such as coastal upwelling systems, the phytoplankton cells (identified by pigment color patterns) behave largely as passive scalars at the mesoscale and that growth, death, and sinking of phytoplankton collectively play at most a marginal role in determining the spectral statistics of the pigment patterns.

## Introduction

Satellite imagery offers the opportunity for simultaneous two-dimensional comparison of biological (pigment) and physical (thermal) variability in the upper ocean. Over the last 2 decades much observational, analytical, and theoretical effort has focused on determining the relative roles of physical advection versus biological growth, mortality, and sinking on horizontal variability or patterns in plankton abundance [e.g., *Steele*, 1978; *Bennett and Denman*, 1985; *Davis et al.*, 1991; *Denman*, 1994]. Attempts to test hypotheses formulating characteristic length scales separating regimes in which physical or biological processes dominate have achieved limited success, primarily because shipboard transects suffer from time-space contamination, vertical-horizontal contamination, and undersampling in the cross-transect direction. Moored sensors provide high-resolution temporal coverage but at the expense of spatial coverage. Satellite sensors provide synoptic two-dimensional coverage resolving scales from 1 km to hundreds of kilometers, multiple realizations in time, and nearly simultaneous sampling of both derived near-surface chlorophyll pigment, from the coastal zone color scanner (CZCS), and sea surface temperature, from the advanced very high resolution radiometer (AVHRR). Principal limitations are that both sensors sample only the surface of the ocean, neither can "see" through clouds, and the CZCS usually provides only one pass per day.

Both the AVHRR sensors and the CZCS sensor have required more than a decade of algorithm development to yield consistent, useful quantitative data, because the ocean signal received by each sensor is only a small fraction of the atmospheric signal, which must be estimated and removed (see *Abbott and Chelton* [1991] for a review of sensor and algorithm development). Careful processing of AVHRR data can yield sea surface temperature rms errors of ±0.5°C for a single image [e.g., *McClain et al.*, 1985], but unfortunately,



Paper number 93JC02149.
0148-0227/94/94JC-02149$05.00.

errors are usually larger because of the lack of high-quality in situ observations for calibration and because of undetected clouds. The comparable rms error for derived chlorophyll pigment from the CZCS is $\pm 0.3$ $\log_{10}$(pigment) [*Gordon et al.*, 1983a]. The scatter is greater at lower (because of signal noise) and higher pigment concentrations [*Brown et al.*, 1985; *Denman and Abbott*, 1988 (hereinafter referred to as DA88)]. The average layer thickness observed (an optical depth) differs for the two sensors: the optical depth for the AVHRR is only a few micrometers because of strong absorption by water, but that for the CZCS is several to tens of meters. AVHRR sensors have been on NOAA TIROS N satellites since 1978; the only CZCS sensor operated on the Ninbus 7 satellite from 1978 to mid-1986. Hence AVHRR and CZCS images even for the same day were obtained from different satellites at different times of the day at different viewing angles, although in this paper we have navigated them onto the same grid. *Strub et al.* [1990, Appendix A] discussed many of the detailed problems that must be dealt with during analysis of the CZCS data.

Careful analysis of AVHRR and CZCS imagery has increased our understanding of mesoscale processes in the upper ocean. Both types of data have been used to study the advection and propagation of near-surface eddies and other features, AVHRR data have been used in mesoscale air-sea interaction studies, and CZCS data have been used to estimate pigment amounts and rates of primary production and how they vary at the mesoscale. Spectrum analysis of satellite imagery promises a compact, quantitative description of near-surface horizontal spatial variability. Moreover, several models and hypotheses that include various physical transport and mixing processes and biological growth, death, and sinking formulations predict certain spectral shapes for both sea surface temperature and chlorophyll pigment (indicating the abundance of phytoplankton). In all cases, differences in spectral shapes between CZCS and AVHRR data are hypothesized to indicate the importance of nonconservative biological processes in determining the spatial patterns of the chlorophyll pigment beyond the advective and diffusive processes in the physical water motions. In reality, the thermal patterns are neither passive nor conserved, because they contribute to the geostrophic currents and they change as a result of solar heating, air-sea heat exchange, and exchange of the surface layer with the deeper ocean (for example, *Swenson et al.* [1992] found from drifter data that cold jets are heated preferentially by about 0.15°C $d^{-1}$ compared with adjacent warmer waters).

Various investigators have performed spectrum analysis on AVHRR and CZCS satellite imagery, using either conventional single-variable analysis of one-dimensional transects sampled from the images or two-dimensional analysis of cloud-free subareas of the images. For ocean color images, *Gower et al.* [1980] obtained an equivalent one-dimensional spectrum (by averaging spectral coefficients in concentric rings in two-dimensional wavenumber space) for one of the visible bands in a Landsat image (180 × 250 km) of the Atlantic Ocean south of Iceland. The log-log plot of the spectrum was roughly linear with a slope of about $-3$, corresponding to a slope of $-2$ for a log-log plot converted from a variance-conserving linear spectrum (where spectral coefficients are summed rather than averaged, thereby conserving variance (DA88)). DA88 obtained (by summing coefficients) a spectral slope of roughly $-2$ for CZCS images of areas off Vancouver Island, Canada, but they were primarily interested, as we are in this paper, in calculating autospectra as one step in the calculation of squared-coherence spectra between pairs of images of the same area but separated in time. For six areas in the Atlantic and Pacific oceans, *Barale and Trees* [1987] calculated average variance spectra from 20 transects in each area with slopes ranging from $-1.0$ to $-2.5$. The spectral shapes were similar to those of DA88 except for the two open ocean areas with the lowest chlorophyll concentrations ($<0.2$ mg $m^{-3}$), for which the log-log spectra were not straight lines but increased upward for wavenumbers greater than about 0.05 (pixels$^{-1}$). The average dimension of their "compressed" pixels was 2.5 km, making the wavenumber roughly equivalent to 0.02 $km^{-1}$. *Smith et al.* [1988] analyzed 48 CZCS images from six areas off southern California. They, like DA88, found that pigment concentrations were approximately log normally distributed. Spectral slopes ranged from about $-2$ to $-3$, but they found a distinct shallowing of the slope at wavenumbers greater than about 0.08 $km^{-1}$. In four comparisons, they found no such change in slope in temperature spectra. They attributed the divergence of the chlorophyll spectra from the temperature spectra to biological processes affecting the chlorophyll pigments at smaller scales. *Burgert and Hsieh* [1989] calculated spectra for transect lines taken on AVHRR data for the area studied by DA88. They obtained straight-line spectra on log-log plots with slopes of about $-2$, but data from the same transect taken on two images 1 day apart were coherent only for wavenumbers greater than about 0.18 $km^{-1}$. Coherence only at small scales is difficult to explain because of image "navigation" uncertainties, surface currents and eddy evolution, and air-sea heat exchanges.

The first objective of this paper is the same as that of DA88: to estimate from sequences of satellite images the rate of decorrelation or change in surface patterns as a function of the time separation between images. We calculate the squared coherence $K_{12}^2(\kappa)$ for broad bands of inverse wavelength $\kappa$ (where the directional spectra have been converted to equivalent one-dimensional spectra). For each wavenumber band (here wavenumber ≡ inverse wavelength), the squared coherence $K_{12}^2(\kappa, \tau)$ values are plotted against the time separation $\tau$ between images, forming the spectral analog of a lagged cross-correlation function $r_{12}^2(0, \tau)$. For this paper we have identified sequences of both CZCS and AVHRR images from the area off northern California that was the site of the Coastal Ocean Dynamics Experiment (CODE-81). We therefore can examine differences in spectral statistics, specifically the time rate of pattern decorrelation between pigment and thermal patterns, that might indicate biological influences on the spatial patterns of chlorophyll pigment. In addition, we can calculate a time-lagged cross-coherence function between pigment and thermal patterns to investigate whether the spectral statistics of the pigment patterns lag those of the thermal patterns, as might be expected in a coastal upwelling regime where high-biomass regions are assumed to develop downstream from the centers of upwelling of nutrient-rich waters.

## Methodology

### Study Area

The study area is the continental margin of northern California that was the region of CODE-81. The CZCS

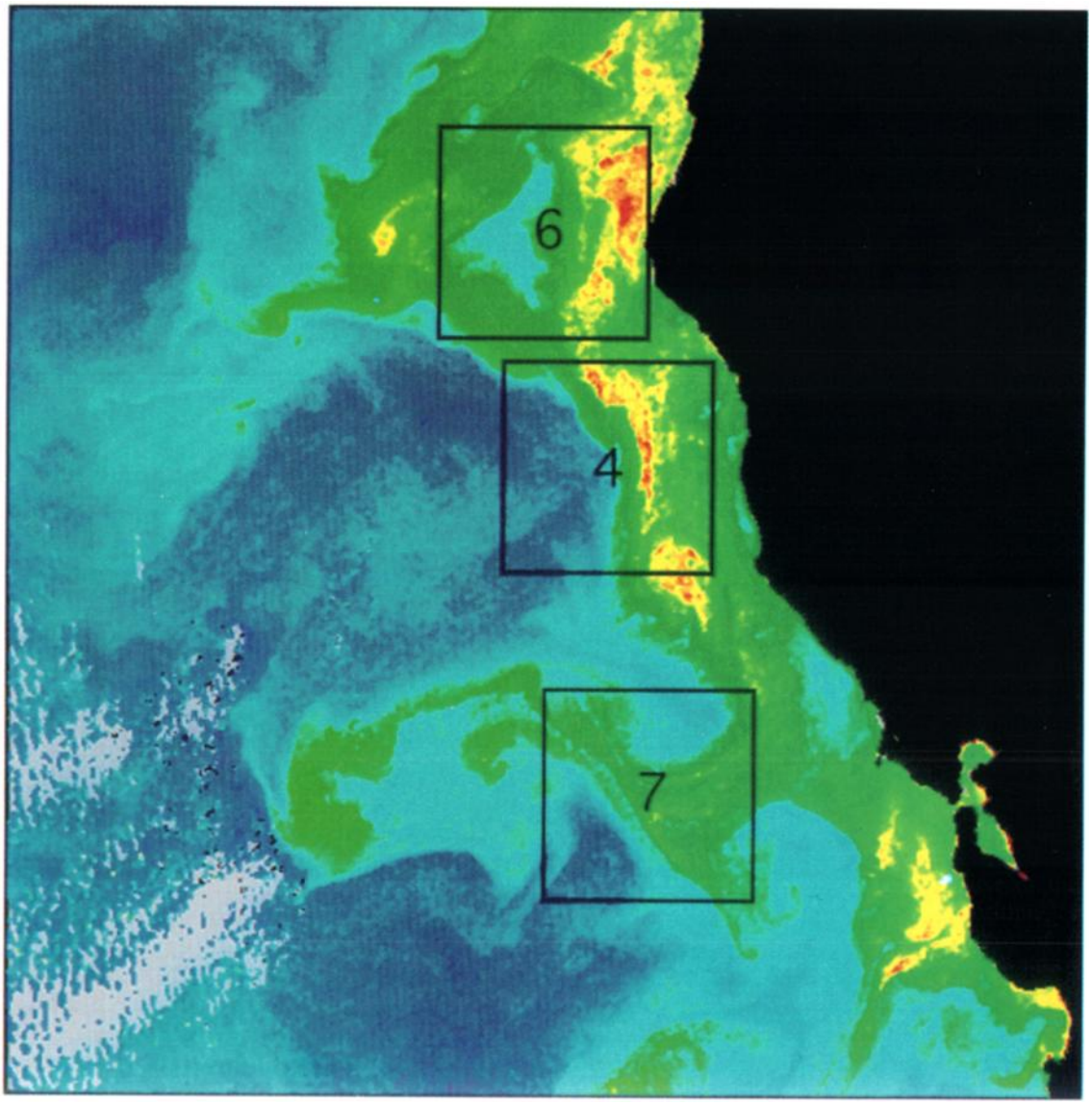


**Plate 1.** CZCS image for Julian day 189, 1981, showing the three 100 × 100 pixel regions used in the analyses: subarea 6, the northern filament; subarea 4, the middle eddy; and subarea 7, the southern filament. The image, an equirectangular projection centered on 39°N, 125°W, represents 512 × 512 square pixels, each 1.1 km on a side (representing 0.01° of latitude). The gray patterning in the lower left is cloud, and the large enclosed bay to the east of subarea 7 is San Francisco Bay.

images, collected at the Scripps Satellite Facility and processed at the Jet Propulsion Laboratory, are cataloged by *Abbott and Zion* [1984]. They were remapped to an equirectangular grid of 512 × 512 pixels centered at 39°N, 125°W, where each pixel is 1.1 km on a side (corresponding to 0.01° of latitude). Phytoplankton pigment concentrations were estimated with the standard algorithms of *Gordon et al.* [1983a, b] and correlated well with shipboard samples ($r^2$ = 0.8, slope = 1.0, $n$ = 11) [*Abbott and Zion*, 1987]. AVHRR images for the same time period were remapped to the same grid and converted to temperatures with standard algorithms. On the basis of absence of cloud cover on repeated days (see below), we eventually chose three subareas (100 × 100 pixels) on which to perform spectrum analysis, and they are shown in Plate 1. Subareas 6 (northern filament) and 7 (southern filament) are located in "active" regimes where persistent upwelling filaments develop from the coast to several hundred kilometers offshore, and subarea 4 (middle eddy) is located in a "quiet" regime between the two centers of upwelling activity.

Although the data were processed using an early version of the CZCS algorithms developed at the University of Miami, the residual errors caused by use of the Rayleigh single-scattering correction and by algorithm "switching" are not important for this analysis. Use of the single-scattering algorithm will cause errors at the low Sun angles which occur at high latitudes during winter. As the analysis was confined to summer, this will not be a significant source of error. Images in which the region of interest lies at the edge of the swath were discarded in part because of the difficulty of atmospheric correction and also because of pixel distortion caused by the large off-nadir view angle. Algorithm switching will manifest itself at small scales; as our analysis will show, successive images are essentially decor-

related at scales less than a few kilometers, and we consider them no further. We removed from analysis all images in which more than a few pixels were contaminated by clouds. Improved algorithms might have reduced the number of images that we discarded, but they would not have significantly altered the statistical results from the images that we analyzed.

### Algorithms for Spectrum Analysis

We followed the basic methodology for statistical and spectrum analyses developed by DA88. In the analysis of the CZCS data, we used log chlorophyll values because they were more nearly normally distributed, a desirable prerequisite for spectrum analysis. A. Dolling of Channel Consulting performed the analyses at the Institute of Ocean Sciences in Sidney, British Columbia, Canada.

First, we examined images visually and checked their frequency distributions for contamination by clouds in order to identify subareas that were clear on several occasions days to weeks apart. Then a 3 × 3 running median filter was applied to all images to remove noise spikes or dropout, and out-of-range points (providing there were only a few) were set to zero (after a least squares fitted $(x, y)$ plane had been removed). We were unable to determine completely objective criteria for rejection of images contaminated by cloud, but we erred on the conservative side by rejecting images with any question of contamination, often after examining the autospectra for excessive variance at high wavenumbers. For example, the CZCS image for Julian day 153 [*Abbott and Zion*, 1984, p. 43] was rejected because of its "speckled" appearance, which showed up as excessive variance at high wavenumbers and which might be attributed to a low viewing angle by the sensor. This speckling sometimes results from switching between the low- and high-chlorophyll bio-optical algorithms used in CZCS processing [*Gordon et al.*, 1983a; *Strub et al.*, 1990, Appendix A]. DA88 showed in their Figure 3 how switching between algorithms can cause a discontinuity in the frequency distribution of chlorophyll values at 1.5 mg $m^{-3}$, the test value for switching algorithms.

We then applied to each image a boxcar filter which set to zero all points outside the subarea. Within each subarea, a cosine taper was applied to the residuals, with a 10% taper at each end of the subarea, first in the east-west direction and then in the north-south direction. A two-dimensional fast Fourier transform (FFT) was then applied to each 512 × 512 image, the only nonzero values being within the subarea. Equivalent variance-conserving one-dimensional spectra were formed by azimuthal summation over concentric rings in wavenumber space, each with radius $\kappa$ and thickness $\Delta\kappa$ (which can be constant or increasing with wavenumber to be constant on a log $\kappa$ axis). Estimates at wavenumbers $\kappa <$ (1/111 km), representing variance at wavelengths longer than the dimension of a subarea, are meaningless and were set to zero.

The squared coherence estimate $K_{12}(\kappa, \tau)^2$ between two images separated in time by an amount $\tau$ represents the correlation between the two images at some wavenumber $\kappa$. Estimates of $K$ were obtained by first computing by FFT the complex cross spectrum between the two images $s_{12}(\kappa) = c_{12}(\kappa) - iq_{12}(\kappa)$, where $c_{12}$ and $q_{12}$ denote the cospectrum and the quadrature spectrum, respectively. They were summed azimuthally to give one-dimensional cospectra and quadrature spectra $C_{12}(\kappa)$ and $Q_{12}(\kappa)$ in several broad wavenumber bands. One-dimensional squared-coherence estimates were then formed:

$$K_{12}^2(\kappa) = \frac{C_{12}^2(\kappa) + Q_{12}^2(\kappa)}{S_{11}S_{22}}$$

Finally, we plotted the squared-coherence estimates $K_{12}^2(\kappa, \tau)$ against the time separation $\tau$ between image pairs to form a time-lagged cross-coherence function for thermal images and chlorophyll pigment images and between thermal and pigment images.

Confidence limits for the autospectra were computed in the standard manner [e.g., *Jenkins and Watts*, 1968] under the assumption that each normalized spectral estimate is a chi-squared variable whose number of degrees of freedom equals the number of raw spectral estimates summed in that wavenumber band. Squared-coherence threshold levels for nonzero significance relative to expected coherence between two random uncorrelated images were estimated as in DA88. We calculated the squared-coherence spectrum between many pairs of synthetic random uncorrelated images with the appropriate spectral shape for the various bandwidths $\Delta\kappa$ that we used. Out of 1000 realizations we chose the one-hundredth highest estimate as the 90% significance level; that is, only 1 of 10 estimates of squared coherence between two random uncorrelated images would be expected to exceed this value.

**Table 1.** Julian Dates and Times in 1981 for the Images Used in This Paper

| Subarea | Type of Imagery | Julian Days and Hours,* UT |
|---|---|---|
| 4 | CZCS | 132, 150, 188, 189, 190, 194, 195 |
| | AVHRR | 18815, 18903, 18915, 18922, 19002, 19116, 19216, 19421, 19502 |
| 6 | CZCS | 188, 189, 190, 195 |
| | AVHRR | 18815, 18903, 18915, 18922, 19002, 19116, 19216, 19421, 19502 |
| 7 | CZCS | 150, 154, 155, 166, 167 |
| | AVHRR | 15315, 15403, 15516, 16504, 16603, 18803,18815, 18903, 18915,18922, 19002, 19102, 19104, 19116, 19203, 19216, 19421, 19502, 19516, 19521 |

*AVHRR 18903 indicates Julian day 189 at 0300 UT.

## Results

### Autospectra

We calculated autospectra for all the images in Table 1 (denoted by Julian day and, for AVHRR, by an additional two digits denoting the hour in UT), but we have plotted in Figure 1 autospectra only for the middle eddy, which had a comparable number of clear images for both CZCS and AVHRR data. The 90% confidence intervals would apply to each individual spectrum where the black dot represents the actual spectral estimate. Except for the lowest few spectral estimates, the estimates were summed in concentric rings in wavenumber space, whose width $\Delta\kappa$ increased exponentially with $\kappa$ so as to be of constant width on a log $\kappa$ plot. The

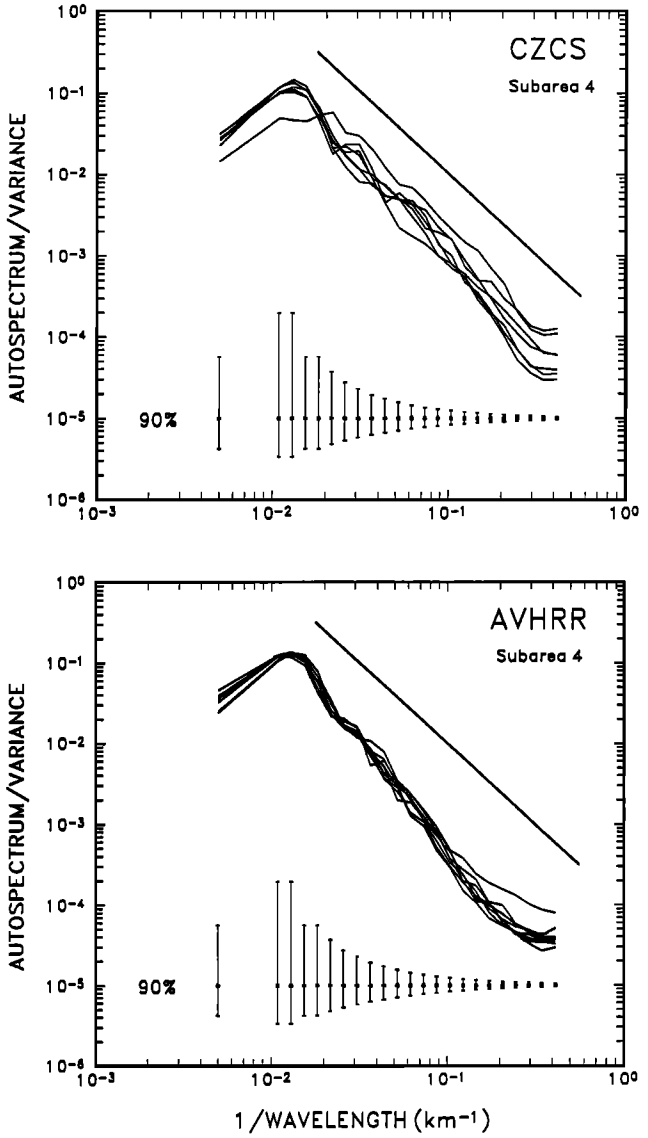


**Figure 1.** Autospectra for the middle eddy (subarea 4) for all images listed in Table 1. (top) CZCS data; (bottom) AVHRR data. The 90% confidence bands plotted across the bottom were calculated assuming that each estimate is a chi-squared variable with the number of degrees of freedom equal to the number of raw spectral estimates summed to obtain the estimate plotted.

AVHRR spectra are more uniform in shape, possibly because they are all from a 1-week period. The one AVHRR spectrum that is anomalously high at high wavenumbers represents an insignificant departure on a variance-preserving $\kappa$ log (spectrum) versus log $\kappa$ plot (not shown). For the CZCS analysis, we included two images from earlier in the year, Julian days 132 and 150, to investigate coherence between pairs with large time separation $\tau$. The one anomalous spectrum (low at low wavenumbers, high at intermediate wavenumbers) is from the image for Julian day 132. This image [*Abbott and Zion*, 1984, p. 37] was also speckled (probably owing to switching between low- and high-chlorophyll algorithms), but we hoped that coherences in band A (large scales, corresponding to wavelengths of 50 to 100 km) would not be significantly contaminated by the high-wavenumber speckling. The last spectral estimate, at an inverse wavelength of about 0.4 km$^{-1}$, usually is higher than the adjacent one, an artifact which is introduced during the 3 × 3 running median filtering. Running median filters applied to single-dimensional series are known to introduce 1-point peaks and valleys, and there are simple algorithms (in one dimension) to correct for the effect [*Kleiner and Graedel*, 1980]. Our results are directed at inverse wavenumbers of less than 0.04 km$^{-1}$ and should therefore be unaffected. The slope of the linear portion of the CZCS spectrum appears to be only slightly steeper than the plotted $\kappa^{-2}$ line; the slope of the AVHRR spectrum appears to be significantly steeper than the $\kappa^{-2}$ line. However, the difference is minor given the different characteristics of the AVHRR and CZCS sensors, and we would caution against interpreting the difference in terms of biological effects on spatial pattern formation.

### Squared-Coherence Spectra

In order to construct the time-lagged autocoherence and cross-coherence functions, we also summed the cospectra and quadrature spectra over broad concentric rings of width $\Delta\kappa$ in wavenumber space before calculating the squared-coherence values. In Figure 2 we show an example of the broad-band squared-coherence function $K_{12}^2(\kappa)$ from the northern filament for CZCS image pairs 1 day and 7 days apart. For a time separation of $\tau$ = 1 day, $K_{12}^2(\kappa)$ for both large scales (band A, wavelengths $\kappa^{-1}$ between 100 and 50 km) and medium scales (band B, between 50 and 25 km) is well above the 90% significance level. For smaller scales (higher inverse wavelengths $\kappa$), the squared coherences are essentially zero, similar to the findings of DA88 for the area offshore from Vancouver Island, roughly 10° latitude north of the CODE-81 study area. For a time separation of $\tau$ = 7 days, $K_{12}^2(\kappa)$ had fallen below (large-scale band) or was equal to (medium-scale band) the 90% significance level. We will thus present lagged coherence functions only for large and medium scales, since at smaller scales most pattern coherence between images appears to be lost after 1 day, consistent with the findings of DA88.

### Auto- and Cross-Coherence Functions

The time-lagged autocoherence function $K_{12}^2(\kappa, \tau)$ is plotted in Figure 3 for the northern filament, the area just offshore of the most active upwelling site and along the path of a recurring offshore-flowing upwelling jet or filament. For large scales (Figure 3, top), squared coherence drops below the 90% significance level for both AVHRR and CZCS patterns after time separations of about 3 days. For medium scales, squared coherence drops below the 90% significance level after only about 2 days. These decorrelation times correspond with those for the nearshore subareas off Vancouver Island in DA88 but are shorter than for the subareas farther offshore where the band A coherences were well above the 90% significance level after the longest time separation ($\tau$ = 7 days) and the band B coherences were just approaching the 90% confidence level.

The middle eddy region, located between the two regions of recurring upwelling jets (Plate 1), might be characterized as more "quiescent" with a longer pattern decorrelation time scale. Figure 4 shows that this is indeed the case: large-scale squared coherences are still above the 90% significance level after time separations of 7 days, and

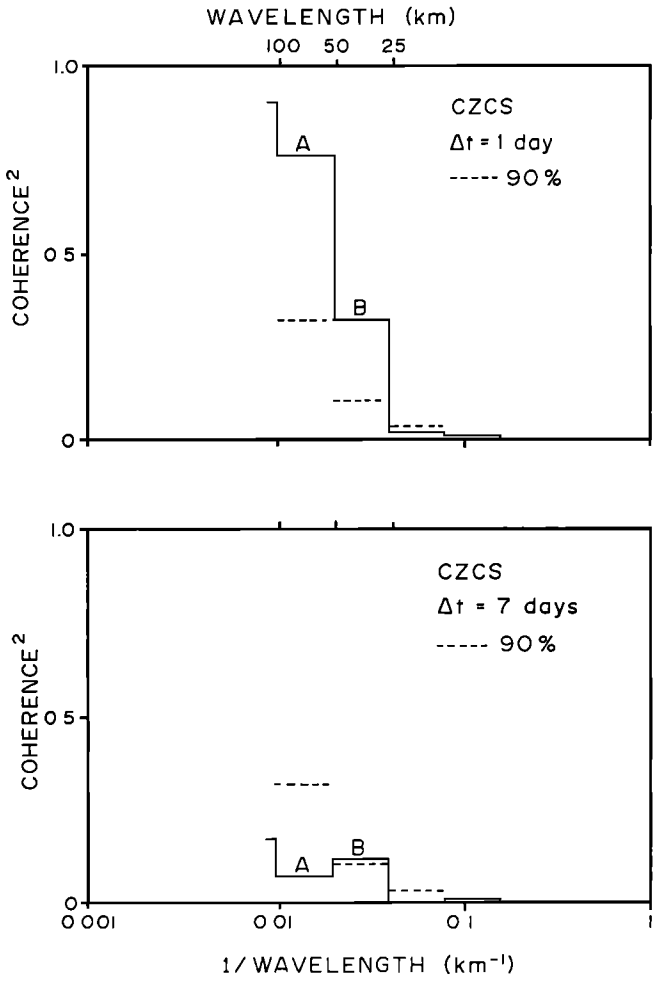


**Figure 2.** Broadband squared-coherence estimates for the northern filament between CZCS images (top) 1 day apart and (bottom) 7 days apart. The 90% significance levels were taken from 1000 coherence calculations between pairs of synthetic random uncorrelated images with a spectral slope of −1.5. We will refer to band A (corresponding to length scales of 50–100 km) as large-scale coherences and to band B (corresponding to length scales of 25–50 km) as medium-scale coherences.

medium-scale coherences are approaching the 90% significance level at that time separation. There is more scatter to these data than to those for the northern filament, and at medium scales the CZCS coherences tend to be lower than the AVHRR coherences at the same time separation. To determine at what time separations the coherences drop below the 90% significance level, we found two clear CZCS images from earlier in the year, on Julian days 132 and 150, which, for CZCS imagery only, allowed us to extend the time-lagged coherence plots in Figure 3 to time separations $\tau$ of up to 63 days. The results, plotted in Figure 5, suggest that for large scales, squared coherence drops below the 90% significance level after about 20 days, and for medium scales, it drops after less than 10 days.

It appears, then, that for a dynamic region of a recurring upwelling jet (northern filament), pattern decorrelation times are at most twice as long as those for a more quiescent region characterized by a relatively stable southward flowing California Current (middle eddy). In both regions, as in DA88, the decorrelation time (value of $\tau$ where the squared coherence drops below the 90% significance level) for large scales is about twice as long as for medium scales, regardless of the region. Our results for the southern filament (plotted in Figure 6), also in a region of a recurring upwelling jet, fall in between. The few CZCS images are consistent with the above categorization: squared coherences fall below the 90% significance levels after time separations of only a few days. The squared coherences for the (many) pairs of AVHRR images drop below the 90% significance level after separations between 3 and 8 days (large scales) and between 1 and 6 days (medium scales).

We now show the time-lagged cross-coherence functions calculated between pairs of AVHRR and CZCS images: the time separation may now be either positive or negative. We might expect CZCS patterns (derived phytoplankton photosynthetic pigments) to lag AVHRR patterns (cold surface temperatures derive from nutrient-rich recently upwelled waters) as the phytoplankton respond to the enriched water and increased light levels. Therefore we have chosen to plot the lagged cross-coherence functions $K_{AC}(\kappa, \tau)^2$ such that positive time separation $\tau$ indicates the AVHRR pattern leading a similar CZCS pattern. In Figure 7 are plotted the functions $K_{AC}(\kappa, \tau)^2$ for the northern filament. The results are clear: in both bands the cross coherences reach a distinct

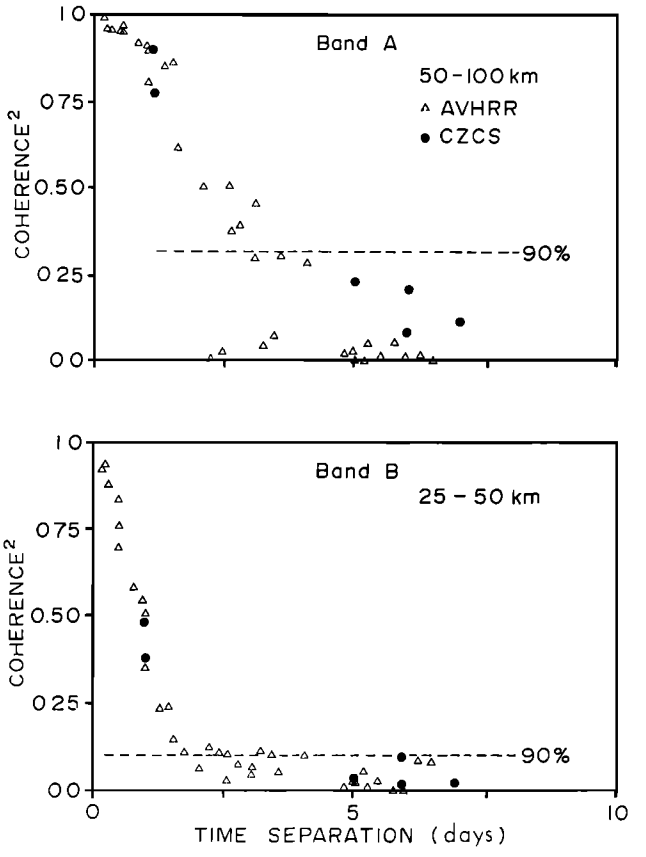


**Figure 3.** Squared-coherence estimates for the northern filament (subarea 6) plotted against time separation $\tau$ between images, to form a temporal lagged coherence function $K_{12}(\kappa, \tau)^2$ for AVHRR and CZCS data separately. The 90% significance levels were estimated as for Figure 2. (top) Large-scale coherences (band A); (bottom) medium-scale coherences (band B).

maximum at zero time lag, with values dropping below the 90% significance levels for time separations greater than about 2 days. Figure 8 shows the same analysis for the middle eddy. Again, there is a clear maximum at zero time lag, but consistent with the autocoherence results in Figure 4, squared coherences remain significant out to lags of 5 to 7 days.

Since the pigment patterns do not lag the thermal patterns in time, it appears that the growth, death, and sinking of the phytoplankton do not significantly affect the statistics of their mesoscale patterns. This coastal regime, although productive, is sufficiently dynamic that the currents and their variability dominate the generation and evolution of the phytoplankton pigment patterns at these spatial scales. However, the lagged cross coherences for the southern filament, plotted in Figure 9, produce unexpected results. At both large and medium scales, significant cross coherence occurs only for lags of 3 days or less (consistent with the northern filament), but the maximum now occurs when pigment (CZCS) patterns lag thermal (AVHRR) patterns by 1 to 2 days. We expect peak concentrations of phytoplankton to occur "downstream" from centers of newly upwelled nutrient-rich water such as that observed near the middle eddy on Julian days 188 and 189 (July 7 and 8, 1981), where the high-pigment area in the CZCS image is clearly adjacent to but not contiguous with the coldest water at the presumed upwelling center [*Abbott and Zion*, 1985, Figures 3 and 4; *Davis*, 1987, Figure 1]. We believe that the results shown in Figure 9 represent the first case in which the spectral

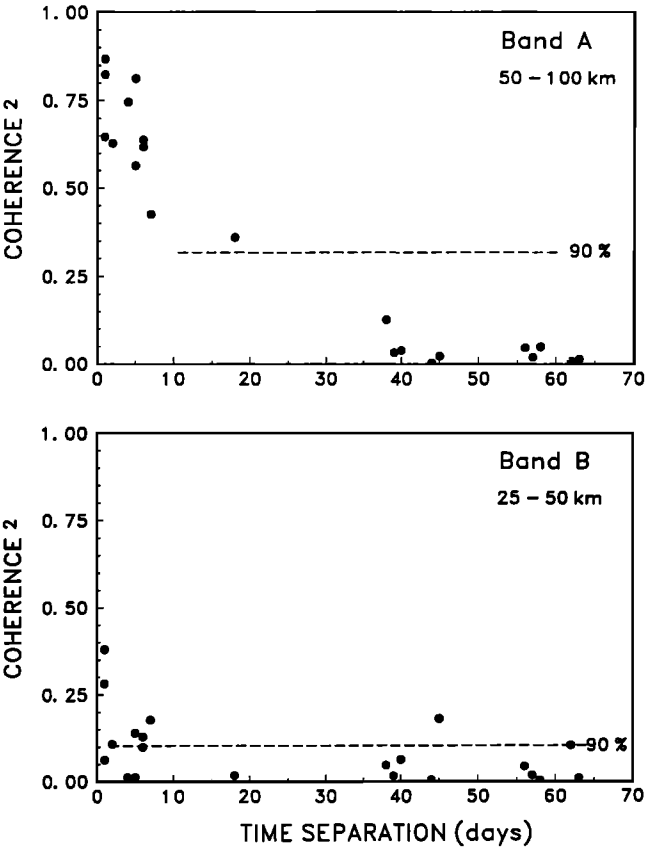


**Figure 5.** The same as Figure 4 (subarea 4) but extended to time separations $\tau$ of up to 70 days (for CZCS data only).

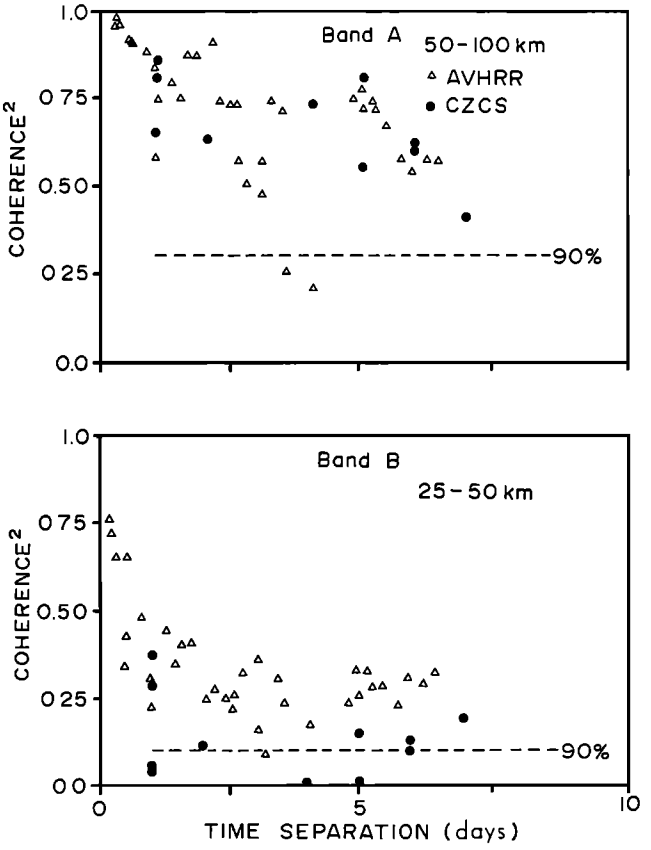


**Figure 4.** The same as Figure 3 but for the middle eddy (subarea 4).

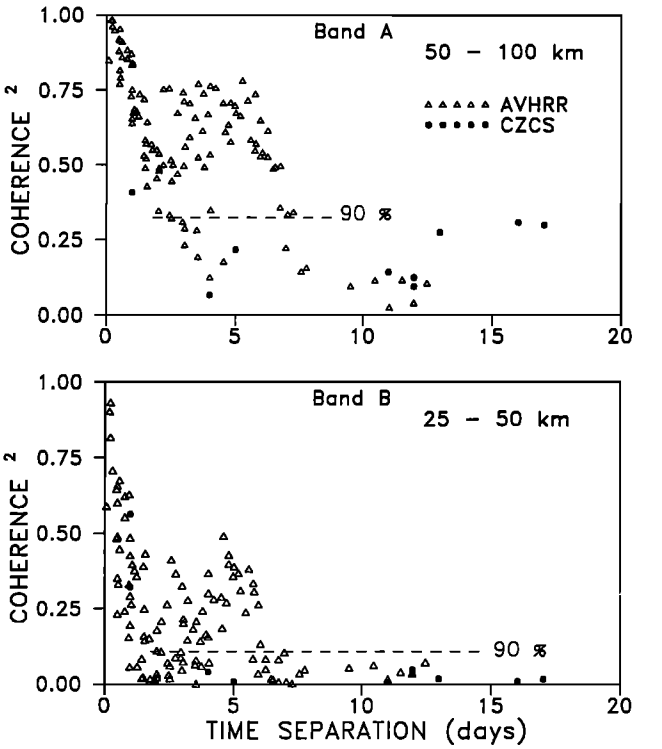


**Figure 6.** The same as Figure 3 but for the southern filament (subarea 7).

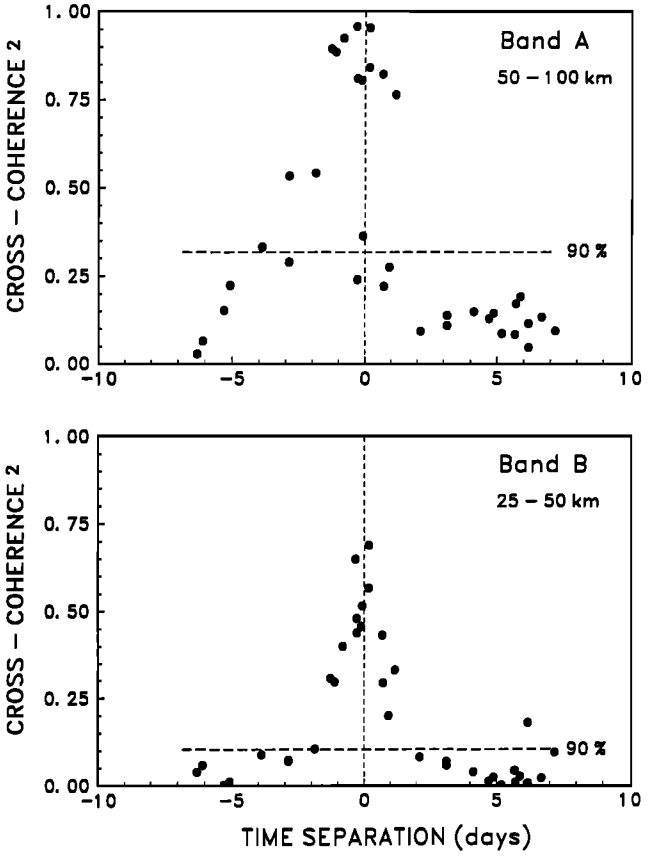


**Figure 7.** Squared cross-coherence estimates for the northern filament (subarea 6) plotted against time separation $\tau$ between images to form a temporal lagged cross-coherence function $K_{AC}(\kappa, \tau)^2$ between AVHRR and CZCS images, with AVHRR leading CZCS. The 90% significance levels were estimated as for Figure 2. (top) Large-scale coherences (band A); (bottom) medium-scale coherences (band B).

statistics of the pigment pattern lag those of the thermal pattern, as indicated by the nonzero time lag for maximum pattern coherence.

## Discussion and Conclusions

The results presented here pertain to three related but distinct scientific problems. The first is the question of to what extent and under what conditions nonconservative biological processes, that is, growth, death, and sinking, can cause horizontal patterns in phytoplankton, which are otherwise passive scalars, to differ from contiguous horizontal patterns in thermal structure as measured by their spectral statistics. The second is the question of what errors or uncertainties are added to regional estimates of phytoplankton production by temporal or spatial variability in dynamic-flow regimes over continental margins. The third is the question of how to use regional decorrelation times and distances in numerical modeling and optimal estimation.

### Importance of Biological Processes

Concerning the first question, up until about a decade ago, horizontal patterns and patchiness in phytoplankton abundance were thought to be controlled by the competing forces of phytoplankton growth enhancing existing spatial variability and turbulent motions diffusing or breaking down the patchiness [e.g., *Steele*, 1978]. Simplistic models with the turbulent motions characterized by a Fickian-type diffusion tended to yield characteristic length scales: at greater scales, growth stabilized and strengthened existing patchiness, and at small scales, turbulent diffusion smeared or dispersed the patchiness so that structures decayed and disappeared. In the last decade, more realistic modeling and theoretical treatment of mesoscale horizontal-flow regimes in the ocean have allowed more explicit examination of the advective dispersal by the flow field of horizontal patterns in passive scalars, both conservative and nonconservative. For example, *Bennett and Denman* [1985] used Lagrangian particle statistics to investigate whether a spatially variable phytoplankton growth rate, either fixed in space or advected by the flow field, can generate and maintain patchiness in a manner not possible for a conserved scalar or a scalar with a spatially uniform growth rate. Their results indicated that patchiness associated with the spatially variable growth rate field was generated initially, reaching a maximum after a time scale associated with the cascade rate for two-dimensional mesoscale turbulence. Thereafter, as the patches advected through more and more eddies, they decayed into a "noisy" distribution retaining no correlation with either the growth rate field or the motion field. *Holloway* [1986] investigated the case of low wavenumber variability in the growth rate in numerically generated quasi-geostrophic horizontal turbulence and with simple closure theory. His results conformed with earlier views: after a

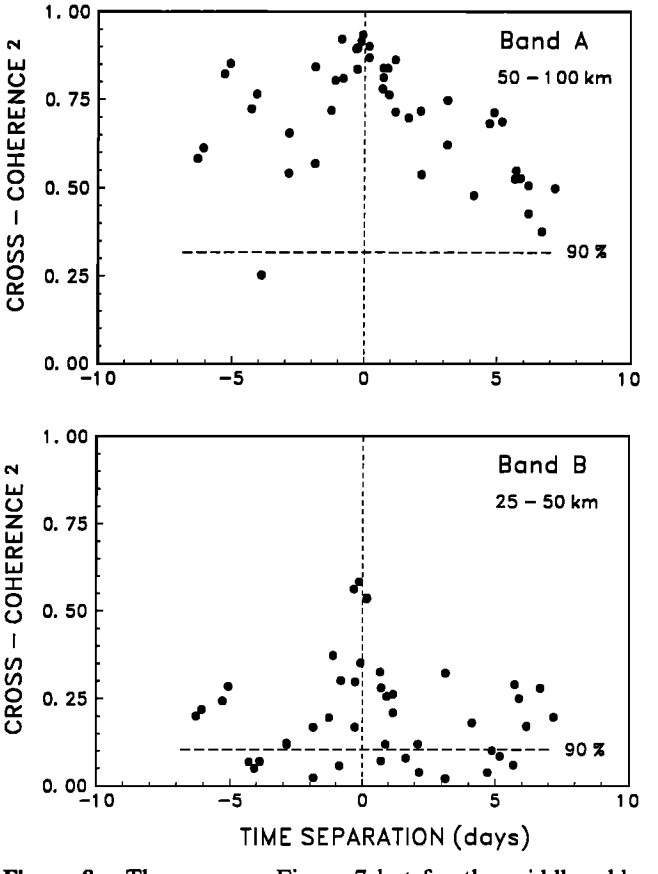


**Figure 8.** The same as Figure 7 but for the middle eddy (subarea 4). AVHRR leads CZCS.

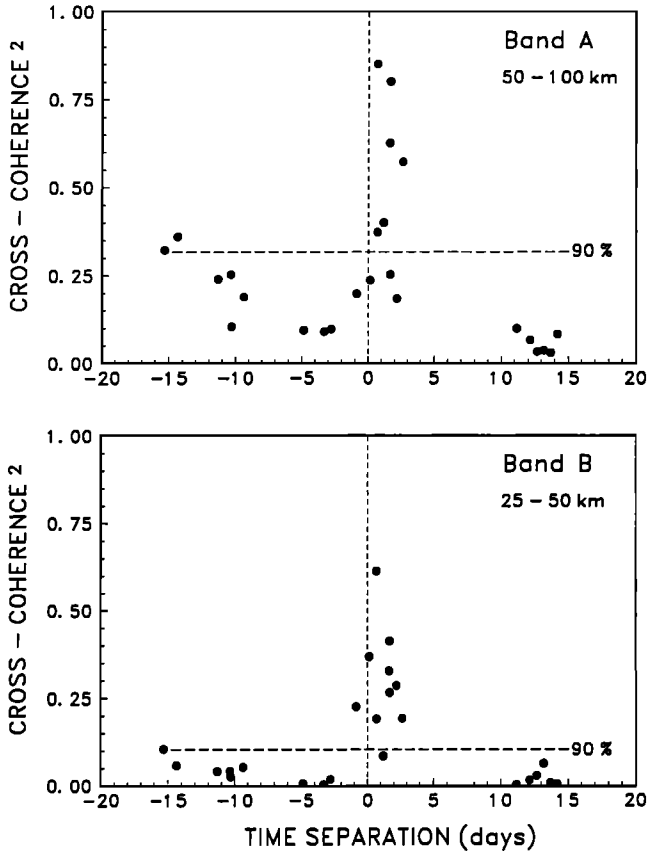


**Figure 9.** The same as Figure 7 but for the southern filament (subarea 7). AVHRR leads CZCS.

reasonable time, an equilibrium was reached at which the large-length-scale growth rate variability generated large-scale patchiness which was transferred by turbulence to shorter-length scales at which variance was dissipated by explicitly modeled diffusion.

The results presented here are generally consistent with the conclusions of *Bennett and Denman* [1985], that is, that the two-dimensional horizontal-motion field in the upper ocean is sufficiently energetic that nonconservative sources and sinks in phytoplankton cannot impose a spatial pattern that will persist through the dispersal characteristics of mesoscale turbulent motion. No significant differences in spectral shape were detected between AVHRR and CZCS imagery. Moreover, in all three subareas, pattern decorrelation times were similar for AVHRR and CZCS data, and in two of the subareas, cross coherences between AVHRR and CZCS patterns peaked at zero time lag, indicating control of the pigment patterns by physical processes. Only in the southern filament was there evidence of biological influence on the spectral statistics of the pigment patterns, where the maximum cross coherences occurred at a lag (CZCS behind AVHRR) of 1–2 days. The southern filament is roughly 50 km farther offshore than the other two subareas, perhaps allowing more time for the phytoplankton to reproduce as the upwelled water is carried offshore in the recurring upwelling jet. *Abbott and Zion* [1987] calculated correlations between mean pigment concentrations in about twenty 16 × 16 pixel boxes in the area denoted by the image in Plate 1. Consistent with our results, they found significant spatial correlation (at zero time lag) at greater distances in the middle eddy and southern filament regions of our study than in the northern filament. These correlations tended offshore to the southwest from the middle eddy region. The only significant correlations at time lags of 5–6 days were roughly along the axis of the southern filament, consistent also with correlation scales for Doppler currents and surface winds in the region. *Campbell and Esaias* [1985] calculated spectra and cross-correlation functions for derived temperature and chlorophyll data from airborne transects of a multichannel ocean color sensor over Nantucket Shoals off Massachusetts. Autospectra were similar to those obtained in this and other studies, and cross-coherence spectra were not significant. Cross-correlation functions were significant at nonzero lags, but both temperature and chlorophyll series showed significant correlation with water depth at much greater lags, indicating that both were dominated by tidal currents advecting water on and off the shallow banks.

We did not explore the coherences for length scales of less than 25 km for several reasons, including different penetration depths of AVHRR and CZCS sensors, different nonconservative processes (such as air-sea heat exchanges and phytoplankton growth, mortality, and sinking), and the estimation [*Gordon et al.*, 1983a] that errors of ±3 km are common in geographic location in CZCS images (and presumably AVHRR images) because of uncertainties in satellite location information. Moreover, searching for complete agreement between models of plankton patchiness and our data would be unwise, because in most models the effects of predation by zooplankton or fish larvae are assumed to be negligible. *Davis et al.* [1991] have made the first steps toward modeling the effects of swimming, prey patchiness, and turbulence on the distribution of predators and find their results to be sensitive to the relative rates of growth and turbulence. Whether such sensitivities in the patchiness of the predator translate into similar sensitivities in the patchiness of the phytoplankton prey has not been well established in observations and obviously will require in situ as well as remote data.

### Importance to Remote Estimates of Primary Production

Concerning the second question, much recent theory and analysis have been directed at obtaining regional estimates of primary production from satellite remote sensing augmented by in situ data [e.g., *Smith et al.*, 1982; *Kiefer and Mitchell*, 1983; *Eppley et al.*, 1985; *Brown et al.*, 1985; *Platt and Sathyendranath*, 1988; *Morel and Berthon*, 1989; *Balch et al.*, 1989a, b]. Our results strengthen a conclusion of DA88 that poorly resolved mesoscale patterns may add significant error to estimates of monthly to seasonal regional production obtained from satellite color imagery. However, because of the high degree of correlation between CZCS and AVHRR on the same or adjacent days, AVHRR images, available from several satellites, might be used to augment sparse ocean color data from a single sensor on a single satellite such as the CZCS or the upcoming sea-viewing wide-field-of-view sensor (SeaWiFS). Analyses like that in the present paper would be required to determine the characteristic pattern decorrelation time for a given region of interest.

### Importance of Data Assimilation Into Numerical Models

Concerning the third problem, data assimilation into numerical models [*Bennett*, 1992] and optimal interpolation

mapping schemes [*Bretherton et al.*, 1976] both require estimates of spatial and/or temporal correlation functions for the region of interest. *Denman and Freeland* [1985] used spatial structure functions from ship-based measurements, and *Chelton and Schlax* [1991] used similar statistics (in their case, variance spectra) to perform temporal interpolation. However, the techniques that we have applied to satellite data should be capable of providing both the temporal and spatial correlation functions for optimal interpolation and assimilation in a particular region.

**Acknowledgments.** We acknowledge financial support from the National Aeronautics and Space Administration, the Office of Naval Research under their Coastal Transition Zone study, and the Canadian Department of Fisheries and Oceans. We thank Jim Gower and three anonymous reviewers for constructive comments on the original draft. Adrian Dolling of Channel Consulting, Victoria, Canada, performed the spectrum analyses.

## References

Abbott, M. A., and D. B. Chelton, Advances in passive remote sensing of the ocean, *U.S. Natl. Rep. Int. Union Geod. Geophys. 1987–1990, Rev. Geophys., 29*, 571–589, 1991.

Abbott, M. R., and P. M. Zion, Coastal zone color scanner (CZCS) imagery of near-surface phytoplankton pigment concentrations from the first Coastal Ocean Dynamics Experiment (CODE-1), March–July 1981, *Tech. Rep. 84-42*, 73 pp., Jet Propul. Lab., Pasadena, Calif., 1984.

Abbott, M. R., and P. M. Zion, Satellite observations of phytoplankton variability during an upwelling event, *Cont. Shelf Res., 4*, 661–680, 1985.

Abbott, M. R., and P. M. Zion, Spatial and temporal variability of phytoplankton pigment off northern California during Coastal Ocean Dynamics Experiment 1, *J. Geophys. Res., 92*, 1745–1755, 1987.

Balch, W. M., M. R. Abbott, and R. W. Eppley, Remote sensing of primary production, I, A comparison of empirical and semi-analytical algorithms, *Deep Sea Res., 36*, 281–295, 1989a.

Balch, W. M., R. W. Eppley, and M. R. Abbott, Remote sensing of primary production, II, A semianalytical algorithm based on pigments, temperature and light, *Deep Sea Res., 36*, 1201–1217, 1989b.

Barale, V., and C. C. Trees, Spatial variability of the ocean color field in CZCS imagery, *Adv. Space Res., 7*(2), 95–100, 1987.

Bennett, A. F., *Inverse Methods in Physical Oceanography*, 346 pp., Cambridge University Press, New York, 1992.

Bennett, A. F., and K. L. Denman, Phytoplankton patchiness: Inferences from particle statistics, *J. Mar. Res., 43*, 307–335, 1985.

Bretherton, F. P., R. E. Davis, and C. B. Fandry, A technique for the objective analysis and design of oceanographic experiments applied to MODE-73, *Deep Sea Res., 23*, 559–582, 1976.

Brown, O. B., R. H. Evans, J. W. Brown, H. R. Gordon, R. C. Smith, and K. S. Baker, Phytoplankton blooming of the U.S. east coast: A satellite description, *Science, 229*, 163–167, 1985.

Burgert, R., and W. W. Hsieh, Spectral analysis of the AVHRR sea surface temperature variability off the west coast of Vancouver Island, *Atmos. Ocean, 27*, 577–587, 1989.

Campbell, J. W., and W. E. Esaias, Spatial patterns in temperature and chlorophyll on Nantucket Shoals from airborne remote sensing data, May 7–9, 1981, *J. Mar. Res., 43*, 139–161, 1985.

Chelton, D. B., and M. G. Schlax, Estimation of time averages from irregularly spaced observations: With application to coastal zone color scanner estimates of chlorophyll concentration, *J. Geophys. Res., 96*, 14,669–14,692, 1991.

Davis, C. O., Future U.S. ocean color missions—OCI, MODIS and HIRIS, *Adv. Space Res., 7*(2), 3–9, 1987.

Davis, C. S., G. R. Flierl, P. H. Wiebe, and P. J. Franks, Micropatchiness, turbulence and recruitment in plankton, *J. Mar. Res., 49*, 109–151, 1991.

Denman, K. L., Physical structuring and distribution of size in oceanic foodwebs, in *Aquatic Ecology: Scale, Pattern and Process*, edited by P. Giller and D. Raffaelli, pp. 377–402, Blackwell Scientific, Boston, Mass., 1994.

Denman, K. L., and M. R. Abbott, Time evolution of surface chlorophyll patterns from cross-spectrum analysis of satellite color images, *J. Geophys. Res., 93*, 6789–6798, 1988.

Denman, K. L., and H. J. Freeland, Correlation scales, objective mapping and a statistical test of geostrophy over the continental shelf, *J. Mar. Res., 43*, 517–539, 1985.

Eppley, R. W., E. Stewart, M. R. Abbott, and U. Heyman, Estimating ocean primary production from satellite chlorophyll: Introduction to regional differences and statistics for the Southern California Bight, *J. Plankton Res., 7*, 57–70, 1985.

Gordon, H. R., D. K. Clark, J. W. Brown, O. B. Brown, R. H. Evans, and W. W. Broenkow, Phytoplankton pigment concentrations in the Middle Atlantic Bight: Comparison of ship determinations and CZCS estimates, *Appl. Opt., 22*, 20–36, 1983a.

Gordon, H. R., J. W. Brown, O. B. Brown, R. H. Evans, and D. K. Clark, Nimbus 7 CZCS: Reduction of its radiometric sensitivity with time, *Appl. Opt., 22*, 3929–3931, 1983b.

Gower, J. F. R., K. L. Denman, and R. J. Holyer, Phytoplankton patchiness indicates the fluctuation spectrum of mesoscale oceanic structure, *Nature, 288*, 157–159, 1980.

Holloway, G., Eddies, waves, circulation, and mixing: Statistical geofluid mechanics, *Annu. Rev. Fluid Mech., 18*, 91–147, 1986.

Jenkins, G. M., and D. G. Watts, *Spectral Analysis and Its Applications*, 525 pp., Holden-Day, Oakland, Calif., 1968.

Kiefer, D. A., and B. G. Mitchell, A simple, steady state description of phytoplankton growth based on absorption cross section and quantum efficiency, *Limnol. Oceanogr., 28*, 770–776, 1983.

Kleiner, B., and T. E. Graedel, Exploratory data analysis in the geophysical sciences, *Rev. Geophys., 18*, 699–717, 1980.

McClain, E. P., W. G. Pichel, and C. C. Walton, Comparative performance of AVHRR-based multichannel sea surface temperatures, *J. Geophys. Res., 90*, 11,587–11,601, 1985.

Morel, A., and J.-F. Berthon, Surface pigments, algal biomass profiles, and potential production of the euphotic layer: Relationships reinvestigated in view of remote-sensing applications, *Limnol. Oceanogr., 34*, 1545–1562, 1989.

Platt, T., and S. Sathyendranath, Oceanic primary production: Estimation by remote sensing at local and regional scales, *Science, 241*, 1613–1620, 1988.

Smith, R. C., R. W. Eppley, and K. S. Baker, Correlation of primary production as measured aboard ship in southern California coastal waters and as estimated from satellite chlorophyll images, *Mar. Biol., 66*, 281–288, 1982.

Smith, R. C., X. Zhang, and J. Michaelsen, Variability of pigment biomass in the California Current system as determined by satellite imagery, 1, Spatial variability, *J. Geophys. Res., 93*, 10,863–10,882, 1988.

Steele, J. H. (Ed.), *Spatial Pattern in Plankton Communities*, 470 pp., Plenum, New York, 1978.

Strub, P. T., C. James, A. C. Thomas, and M. R. Abbott, Seasonal and nonseasonal variability of satellite-derived surface pigment concentration in the California Current, *J. Geophys. Res., 95*, 11,501–11,530, 1990.

Swenson, M. S., P. P. Niiler, K. H. Brink, and M. R. Abbott, Drifter observations of a cold filament off Point Arena, California, in July 1988, *J. Geophys. Res., 97*, 3593–3610, 1992.

M. R. Abbott, College of Oceanic and Atmospheric Sciences, Oceanography Administration Building 104, Oregon State University, Corvallis, OR 97331-5503.

K. L. Denman, Department of Fisheries and Oceans, Institute of Ocean Sciences, P. O. Box 6000, Sidney, British Columbia, Canada V8L 4B2.

(Received October 30, 1992; revised May 17, 1993; accepted August 4, 1993.)